# Magnonic minibands in antidot lattices with large spin-wave propagation velocities

S. Neusser,[1] G. Duerr,[1] S. Tacchi,[2] M. Madami,[2] M. L. Sokolovskyy,[3] G. Gubbiotti,[2,4] M. Krawczyk,[3] and D. Grundler[1,*]

[1]*Lehrstuhl für Physik funktionaler Schichtsysteme, Technische Universität München, Physik Department, James-Franck-Str. 1, D-85747 Garching b. München, Germany*

[2]*CNISM, Dipartimento di Fisica, Universita di Perugia, Via A. Pascoli, I-06123 Perugia, Italy*

[3]*Surface Physics Division, Faculty of Physics, Adam Mickiewicz University, Umultowska 85, Poznań PL-61-614, Poland*

[4]*Istituto Officina dei Materiali del CNR (CNR-IOM), Unitá di Perugia, c/o Dipartimento di Fisica, Via A. Pascoli, I-06123 Perugia, Italy*

(Received 27 February 2011; revised manuscript received 4 May 2011; published 28 September 2011)

Antidot lattices fabricated from permalloy thin films have been investigated by all-electrical spin-wave spectroscopy and Brillouin light scattering. Periodic arrays of 120-nm-diameter nanoholes have been prepared using focused ion beam etching. The periodicity of the square lattices was varied from 300 to 4000 nm. By applying an in-plane field of 40 mT, we discover surprisingly large spin-wave velocities of up to 6 km/s for a periodicity <400 nm. Using micromagnetic modeling and the further-developed plane wave method, we show that edge excitations at neighboring holes couple and form an allowed miniband supporting fast spin waves. By varying the orientation of the magnetic field we control the miniband characteristics. The coupling of edge modes opens interesting perspectives for magnonic crystals.

DOI: 10.1103/PhysRevB.84.094454 PACS number(s): 75.40.Gb, 75.30.Ds, 75.75.−c, 75.78.−n

## I. INTRODUCTION

Ferroic materials which are patterned on the nanoscale are expected to provide enhanced functionality in information processing and sensor applications.[1] In particular, ferromagnetic nanostructures have generated a large interest where collective spin excitations [i.e., spin waves (SWs)] are expected to transmit and process information. The research field aiming at the control and manipulation of SWs (or magnons) is now called magnonics.[2] Spin-wave-based logic is envisioned which offers parallel computing, low power consumption, as well as working frequencies in the gigahertz regime.[3,4] For this, however, it is crucial to overcome the relatively small group velocities $v_g$ of SWs. Ultimate control and functionality are expected from a so-called magnonic crystal (MC) where an artificially tailored band structure for SWs is formed with allowed minibands and forbidden frequency gaps.[5,6] The search for MCs is also stimulated by the successful implementation of photonic, plasmonic, and phononic crystals in dielectric, metallic, and semiconducting materials, respectively.[7–9] Periodic arrays of nanoholes or nanopitches have led to the functionalization of the corresponding materials. Allowed minibands and forbidden frequency gaps have been provoked by coherent backscattering of the corresponding waves from holes or pitches.

Magnonic crystals have entered the focus of experimental and theoretical research in nanoscience only recently. Pioneering experiments performed on arrays of magnetic nanowires have successfully demonstrated miniband behavior and forbidden frequency gaps.[10–15] However, severe obstacles and drawbacks have been reported which hinder potential applications of MCs in microwave electronics. The relevant issues are the following: First, SW propagation velocities $v_g$ are much smaller if compared with unstructured films, suggesting slow signal processing in nanostructures.[10–16] For an individual magnetic element of lateral dimension $l$, the smallest excitable wave vector is on the order $\pi/l$. This is due to spin-wave quantization.[17] For $1\ \mu\text{m} > l > 10$ nm, theory predicts that SWs reside in an intermediate regime between dipolar-dominated and exchange-dominated SW excitations.[18] For SWs in such nanostructures, group velocities are particularly small. To obtain large $v_g$, MC unit cells were of micrometer[19] and even millimeter dimensions,[20] making miniaturization impossible. Second, inelastic light scattering [i.e., Brillouin light scattering (BLS)] was used to probe the SW propagation across the periodic arrays.[10,11,15,21] Here it is an experimental challenge to provide such a large wave-vector resolution that $v_g$ can be measured close to $k = 0$, which has been suggested to be particularly interesting for MCs.[22] Third, an important improvement has been achieved by MCs consisting of a complex unit cell with two different ferromagnetic materials.[21] Here, group velocities are up to 4 km/s at $\mu_0 H = 0$ mT [extracted from Fig. 2(a) of Ref. 21 at $k \approx 1.2 \times 10^5$ rad/cm]. However, the device fabrication is challenging. Two exposure and material deposition steps are needed and they have to be aligned precisely on the nanoscale.

In this paper we present an approach on how to generate magnonic minibands and large $v_g$ by employing periodic nanoholes in a single permalloy ($Ni_{80}Fe_{20}$) thin film. The antidot lattices (ADLs) [Fig. 1(a)] have been prepared by focused ion beam etching, which has allowed us to create edge-to-edge separations down to 180 nm. Hereby, we have been able to generate MC behavior with strikingly large $v_g$. Our results suggest that localized modes residing close to the edges of holes are coupled dynamically. The strong dipolar interaction between edge modes is attributed to the contiguous ferromagnetic material between the holes' edges, providing a large magnetic susceptibility. The interaction is larger when compared with the inverse structure of an array of isolated magnetic ellipses, which are stray-field coupled via air gaps with small susceptibility.[23] The strong coupling gives rise to a pronounced miniband. Being similar to a tight-binding approach, the coupling mechanism is in contrast to the mechanism based on coherent backscattering from periodic holes and pitches, as reported for photonic, plasmonic, and phononic crystals.[7–9] To explain our findings microscopically we perform micromagnetic simulations and, in particular, develop further the so-called plane wave method (PWM),

 

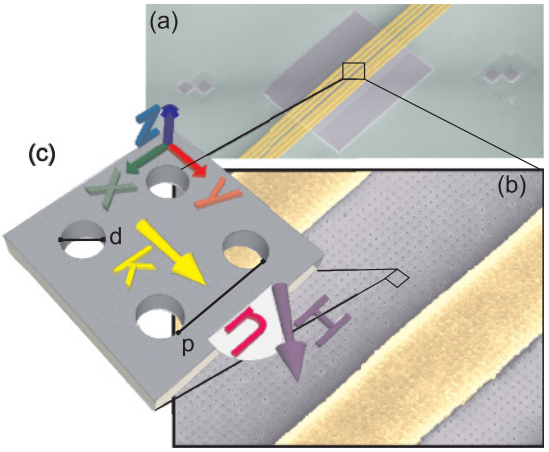


FIG. 1. (Color online) (a) and (b) Scanning electron microscope image of the antidot lattice in permalloy with integrated coplanar waveguides (CPWs). The holes have a diameter of $d = 120$ nm and are arranged on a square lattice of period $p = 300$ nm, as highlighted by the magnified image. (c) Sketch of the device geometry displaying relevant parameters: magnetic field **H**, angle $\eta$, and wave vector **k** addressed by the CPWs.

which originally was restricted to three-dimensional (3D) magnetic systems.[24] The experimental findings and theoretical approach are relevant to design and optimize the functionality of two-dimensional (2D) MCs.

The paper is organized as follows: In Sec. II the sample preparation and the experimental techniques are described. In Sec. III A, we investigate the dependence of the group velocity $v_g$ on the lattice periodicity $p$. Based on this, in Sec. III B, we discuss in detail the fast SW propagation by dipolar coupling of edge modes in the antidot lattice of periodicity $p = 300$ nm. The spin-wave dispersion of the edge mode as measured by BLS and modeled by micromagnetic simulations is reported in Sec. III C. Finally, in Sec. IV, the plane wave method is presented to verify and interpret results in further detail.

## II. EXPERIMENT

### A. Sample preparation

A permalloy mesa was fabricated using optical lithography and electron gun evaporation. Base pressure was $2 \times 10^{-7}$ mbar. During evaporation we achieved $8 \times 10^{-7}$ mbar. The thickness of the permalloy was $\delta = 25 \pm 3$ nm, as determined by atomic force microscopy. We measured the Gilbert damping of the permalloy to be $\alpha = 0.005 \pm 0.002$ following the vector-network-analyzer (VNA) ferromagnetic resonance technique.[25] A periodic array of nanoholes (i.e., an ADL) was fabricated in the permalloy mesa using focused ion beam (FIB) etching. The current was 150 pA and the exposure duration was 8 to 9 ms. The total exposure duration was between 5 and 30 minutes. We fabricated different ADLs. From sample to sample the ADL periodicity $p$ of the array of nanoholes [Fig. 1] was changed from 300 to 4000 nm while the hole diameter was $d = 120 \pm 10$ nm for all samples. This was checked by scanning electron microscopy. We chose in particular FIB etching because it allowed us to stay with one-and-the-same hole diameter for the different periodicities, which we varied by more than a factor of ten. Electron beam lithography would have been challenging because a detailed proximity correction would have been required for the smallest $p$. Subsequently, the samples were capped by a 15-nm-thick insulator ($SiO_2$). Using a double-layer photoresist and optical lithography, two parallel coplanar waveguides (CPWs) were integrated onto the insulator above each ADL by lift-off processing. To minimize ohmic losses it was found crucial to fabricate the CPW from a 80-nm-thick silver layer, capped with 25-nm-thick gold.

### B. All-electrical spin-wave spectroscopy

Coplanar waveguides (CPWs) were integrated [Figs. 1(a) and 1(b)] to investigate spin-wave spectra and group velocities $v_g$ by all-electrical spin-wave spectroscopy (AESWS).[26–28] For AESWS we use two collinear CPWs (i.e., sender and receiver) with an inner conductor width of 2 $\mu$m and a spin-wave propagation distance of $s = 12$ $\mu$m. In this work the CPWs are thus sensitive at small SW wave vectors $k$ close to about $10^4$ rad/cm.[28] The microwave output power of the VNA is small so that we address the linear regime. For the following discussion we will attribute $k_{CPW} = 1 \times 10^4$ rad/cm to the CPWs used in this work. The CPWs are collinear with and define the $x$ axis such that the transferred wave vector is orientated along the $y$ axis [Figs. 1(b) and 1(c)]. Via AESWS, we measure the group velocity $v_g$ at $k_{CPW}$ in the following way:[28] By continuous wave excitation at frequency $f$, a particular SW wave vector $k$ is selected via the SW dispersion $f(k)$. The phase $\Phi$ of the SW at the receiver site is given by $\Phi = k(f)s$. Sweeping $f$ changes $\Phi$. The phase $\Phi$ enters the inductive signal picked up at the second CPW with a VNA. Measuring the change of $\Phi$ and considering $\partial f/\partial \Phi = s^{-1}\partial f/\partial k$, we extract the slope of the relevant SW dispersion from the measured transmission signal between the two CPWs. The slope corresponds to $v_g$. The experiments are performed for different in-plane magnetic fields **H** using a microwave probe station equipped with a crossed pair of field coils.[29] For $\eta = 0^\circ$, the magnetic field **H** is collinear with the $x$ axis. Let $\phi$ denote the misalignment between $x$ axis and the ADL.

### C. Brillouin light scattering

Brillouin light scattering is used to measure the dispersion of thermally excited spin waves with wave vectors $k$ up to $2 \times 10^5$ rad/cm.[23] To study the SW dispersion frequency $f(k)$ for $k \leqslant 2 \times 10^5$ rad/cm, we use BLS on nominally identical samples without insulator and CPW, as discussed in Ref. 23. BLS spectra were measured by using a Sandercock $(3 + 3)$ pass tandem Fabry-Perot interferometer. 200 mW of solid state laser light (wavelength 532 nm) were focused onto the antidot surface through a camera objective. Because of the photon-magnon conservation law of momentum in the scattering process, the in-plane component of the spin wave wave vector $k$ is linked to the incidence angle of light $\theta$ via $k = (4\pi/\lambda)\sin\theta$. By sweeping the incident angle of the light, we measure the SW dispersion (frequency vs wave vector). Experiments are performed in the magnetostatic surface-wave configuration where $k$ is perpendicular to the direction of the in-plane magnetic field $H$.

### D. Simulations and theoretical modeling

We employ micromagnetic simulations with 2D periodic boundary conditions to model local SW excitation in the array of periodic holes.[30] Simulation parameters are saturation magnetization $M_s = 760$ kA/m, thickness $\delta = 22$ nm, and exchange constant $A = 1.3 \times 10^{-11}$ J/m. The field $H$ is orientated 1° off the high-symmetry direction of the ADL to avoid artifacts. Field pulses excite SWs in the linear regime up to $f = 50$ GHz. The simulation time is 10 ns. For simulations at $k = 0$, we simulate a single ADL unit cell subdivided into square simulation-mesh cells with a lateral size of 3.25 nm. Each simulation-mesh cell has a transverse width of 11 to 14 nm. Micromagnetic simulations also allow us to model the specific spin-wave dispersion of a given ADL.[30] For such simulations with $k > 0$, we consider a single row consisting of up to 65 ADL unit cells in the $y$ direction. The lateral size of the simulation-mesh cells is between 8 and 20 nm, depending on $p$. The spatial extent of the field pulse is $2p$ and the peak value of the field pulse amounts to 0.1 to 0.2 mT. A 2D fast Fourier transform yields the dispersion relation $f(k)$. From its slope at $k = k_{CPW} = 1 \times 10^4$ rad/cm, we extract the simulated value of $v_g$.

To systematically calculate spin-wave dispersions at high accuracy we use the semianalytical plane wave method (PWM).[24] This approach helps us to understand the different modes occurring in the ADLs and their systematic dependencies on geometrical parameters. The PWM has been established for the calculation of SWs in 3D systems consisting of two ferromagnets in the saturated state. This is a configuration in which spatial inhomogeneity of the static demagnetizing field either does not occur or is negligible.[24] In the present study we have adapted the PWM to the calculation of magnonic spectra of 2D ADLs with an in-plane external magnetic field. This has required the consideration of nonmagnetic material (i.e., the holes), the modification of the dipolar field calculation method, and the conduction of many numerical tests to verify the correctness of the method. Details on the methods will be given in Sec. IV.

## III. RESULTS AND DISCUSSION

### A. Classification of propagating modes in antidot lattices of different periodicity

In Fig. 2(a) the gray-scale plot shows experimental spectra obtained on the ADL with the smallest periodicity $p = 0.3$ $\mu$m. The strength of $H$ is varied at $\eta = 1°$. The graph in Fig. 2(a) depicts the signal amplitude $a_{11}$ measured on a single CPW in the reflection configuration. Black color indicates an SW resonance. Here, both standing as well as propagating modes are resolved.[28] In Fig. 2(a) BLS data taken at $k = 0$ are also depicted for comparison. In Fig. 2(b), micromagnetic simulations are depicted assuming $k = 0$ and modeling the reflection measurement. We find a one-to-one correspondence between the simulated and measured modes. The graph of Fig. 2(c) depicts the real part of the transmission amplitude $a_{12}$ measured between the two collinear CPWs. From comparison of Fig. 2(a) with Fig. 2(c), we find that only the low-frequency branch labeled i exhibits partly a white contrast in the transmission data. The single spectrum

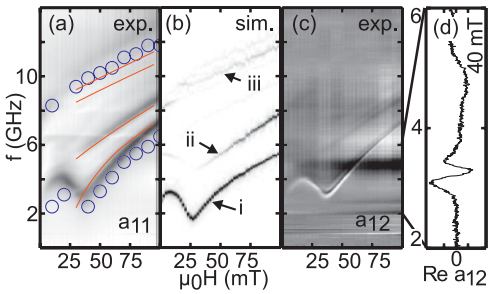


FIG. 2. (Color online) Experimental data taken at $\eta = 1°$ on an ADL with $p = 0.3$ $\mu$m: (a) AESWS amplitude $a_{11}$ in reflection configuration (gray-scale plot, where dark color denotes an SW resonance) and BLS data at $k = 0$ (open circles). Thin solid lines are results of the PWM calculations (see text). (b) Micromagnetic simulation data for $k = 0$ related to the reflection configuration. (c) AESWS real part $a_{12}$ in transmission configuration. Black and white contrast oscillations indicate a phase change due to SW propagation. (d) Single spectrum of the AESWS data (real part) in transmission configuration for $\mu_0 H = 40$ mT.

at $\mu_0 H = 40$ mT in Fig. 2(d) shows that the signal amplitude oscillates between positive and negative values as a function of frequency. This corresponds to an oscillating black-white contrast in Fig. 2(c) near the SW resonance of mode i. It provides evidence of the propagation of this mode between the two CPWs. The oscillating contrast is due to the phase change accumulated along the path by the propagating SW. The resonance frequency of mode i is found to take a minimum at $\mu_0 H \approx 30$ mT. This is the anisotropy field beyond which the magnetization $\mathbf{M}$ of the ADL starts to align with the applied field $\mathbf{H}$. All the further modes at higher frequency are not found to propagate.

Before we discuss the propagation velocities extracted from the transmitted signal $a_{12}$, it is instructive to discuss the magnetic anisotropy of SW modes in a square lattice of nanoholes, as considered here. For this we address again the ADL with the smallest periodicity $p = 0.3$ $\mu$m and the angular dependence of its lowest-frequency mode i. In Fig. 3(a), the solid line represents the measured resonance frequency $f$ in reflection configuration for different $\eta$ at $\mu_0 H = 40$ mT. A minimum of $f = 2.9$ GHz is found at $\eta = 1°$ (i.e., $\eta \neq 0°$). We find that this marks the direction where $H$ is collinear with the ADL unit cell edge (i.e., a high-symmetry direction). We thus attribute $\phi = 1°$ to the misalignment angle of the ADL with respect to the $x$ axis. Note that $f$ varies significantly if $\eta$ is changed by a few degrees only. The precise alignment of $\mathbf{H}$ is crucial for the phenomena discussed in this article.

Next, we use AESWS in the transmission configuration to quantify $v_g$. The solid circles in Fig. 3(a) are for $v_g$ obtained on mode i at $\mu_0 H = 40$ mT. The largest $v_g$ for $p = 0.3$ $\mu$m is observed at $\eta = 1°$, coincident with the minimum frequency $f = 2.9$ GHz. It amounts to $v_g \approx 6.0$ km/s, which is a large value if compared to both earlier results found in nanostructured magnetic devices and in plain films. The value strongly decreases when varying $\eta$; that is, when $\mathbf{H}$ becomes misaligned with the ADL unit cell edge. For $\mu_0 H = 40$ mT, the plain-film group velocity is measured (calculated) to be $v_g = 4.8$ km/s ($v_g = 4.4$ km/s) at a frequency of $f = 6.0$ GHz and $k = k_{CPW}$. Importantly, we find that, for $\mathbf{H}$ aligned with the

unit cell axis, the propagation velocity in the nanostructured ADL is of the same order as in the plain film if the same external field is applied. To compare at a given frequency, one has to keep in mind that, at $k = k_{CPW}$, the minimum frequency for $H = 0$ amounts to $f = 2.87$ GHz for the plain film. Here, $v_g = 8.9$ km/ns. This value reflects the fact that the plain-film SW propagation velocity is inversely proportional to the frequency.[18]

We studied $v_g$ for propagating modes in antidot lattices of different periodicity $p$ to understand the significance of this remarkably high value of $v_g$. It has already been reported that ADLs with mesoscopic lattice constants support different SW modes.[31–34] The characteristic eigenfrequencies and spin-precession profiles depend on the lattice symmetry and orientation of the in-plane magnetic field with respect to high-symmetry directions.[35] In Fig. 3(b), $v_g$ measured by AESWS on ADLs with different $p$ are depicted as circles. We summarize data of $v_g$ measured for small misalignments of $H$ with the ADL primitive vectors (i.e., $\eta - \phi = 1^\circ$ to $2^\circ$). These angles $\eta$ are intentionally chosen to compare with simulations later on which must be performed at $\eta - \phi = 1^\circ$ to exclude artifacts. Note that the values in Fig. 3(b) are thus slightly below the maximum achievable $v_g$ [see, e.g., those presented in Fig. 3(a)]. $v_g$ for $p = 0.3$ $\mu$m is of comparable

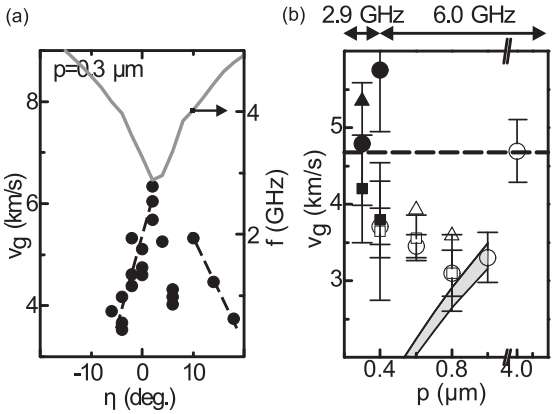


FIG. 3. (a) Eigenfrequency $f$ (solid line, right axis) of the low-frequency mode of the ADL with $p = 0.3$ $\mu$m. $f$ is shown as a function of angle $\eta$ for $\mu_0 H = 40$ mT. Symbols show the corresponding group velocities $v_g$ (left axis) measured at $k_{CPW} = 10^4$ rad/cm. The broken lines are to guide the eye. (b) Group velocities $v_g$ at $k_{CPW} = 10^4$ rad/cm of propagating modes in ADLs with different $p$. The values have been obtained for $2^\circ \leqslant \eta \leqslant 3^\circ$ by AESWS (circles) and micromagnetic simulations (squares) at $\mu_0 H = 40$ mT and $k = k_{CPW} = 10^4$ rad/cm. The horizontal dashed line indicates the plain-film value. At $p = 0.4$ $\mu$m we find two modes of different eigenfrequency which both propagate with a characteristic but different $v_g$. We explain this by a transition in the ADL behavior at this value of $p$: below (above) $p = 0.4$ $\mu$m, the propagating mode is found to exhibit an eigenfrequency $f = 2.9$ (6.0) GHz indicated by the solid and open symbols (see text). At $p = 0.4$ $\mu$m these modes coexist in the experiment, but are not well separated. The group velocities obtained have a large error and are not considered for detailed analysis. Triangles indicate $v_g$ predicted by PWM (given for $\eta = 1^\circ$, see text). The gray shaded area represents group velocities calculated using the nanowire model for $25 \leqslant \delta \leqslant 28$ nm (see text).

magnitude as the unpatterned film value ($v_g = 4.8$ km/s at 40 mT) depicted as the dashed line in Fig. 3(b). For the ADL with $p = 0.4$ $\mu$m a transition is resolved; this is the only sample where two propagating modes are found to coexist. This makes it difficult to extract a value of $v_g$ and errors are large. At $p \approx 4$ $\mu$m the ADL exhibits the same $v_g$ as the plain film. We observe the minimum $v_g = 3.2$ km/s at $p = 0.8$ $\mu$m. It is now interesting that the eigenfrequencies of the prominent modes which propagate through the lattice depend also on $p$. It is important that the frequency $f$ of the propagating mode at $p = 0.3$ $\mu$m with the largest $v_g$ is $f = 2.9$ GHz. For $p > 0.4$ $\mu$m we find $f \approx 6$ GHz for the propagating mode. The purpose of this paper is to explain the strikingly large velocities $v_g$ at $p = 0.3$ $\mu$m and the significant change in the resonant frequency of the propagation mode. We do not discuss details of the mode coexistence occurring at $p = 0.4$ $\mu$m.

To explain the high $v_g$ of the propagating mode at $p = 0.3$ $\mu$m ($\eta = 1^\circ$), we investigate microscopic details of the excitations using simulations and semianalytical approaches. Figure 4(a) illustrates the spatial SW profile of the lowest-frequency excitation, labeled i in Fig. 2(b). Regions of large spin-precession amplitude at $f = 2.9$ GHz reside close to the edges of the holes. Such modes are known as edge modes; in single elements they are named end modes.[12,36] These edge excitations are localized in SW potential wells formed by the demagnetization field $H_d$ close to the edges of the holes. Interestingly, it is found that, at $p = 0.3$ $\mu$m, excited regions at neighboring holes overlap with nonzero amplitude in between the holes. SW propagation can occur from hole to hole through the ADL. This is in contrast to the ADL with $p = 0.8$ $\mu$m [Fig. 4(b)], where the edge excitations of the individual holes are found to be separated by regions of zero precession amplitude. In this scenario, propagation is suppressed for the edge mode. Instead, the higher-frequency mode (i.e., the extended mode at 5.6 GHz) propagates. The corresponding precession profile is depicted in Fig. 4(c). For $p \geqslant 0.8$ $\mu$m, this mode has already been extensively studied in the literature.[28,32] It is known to extend through the lattice in parallel channels of large spin-precession amplitude formed perpendicular to the field. The mode has zero precession amplitude close to the edges of the holes. In Ref. 28 a nanowire model has been introduced to calculate the corresponding SW dispersion. Convincingly, the group velocities measured at $p = 0.8$ and 1.0 $\mu$m lie on the curves in Fig. 3(b), which reflect the nanowire model (solid lines) for film thicknesses $\delta = 25$ to 28 nm. For our data at small $p$ this nanowire model is not found to be valid anymore. To understand the significant changes in the profiles of propagating modes between $p = 0.3$ and $p = 0.8$ $\mu$m in more detail, we analyze the internal field distribution and coupling of the edge excitations localized in the SW wells.

### B. Strong dipolar coupling of edge modes

Analyzing the demagnetization field $H_d$ along the solid line (A–B) of Fig. 4(a) yields a strong peak-to-peak variation $\mu_0 \Delta H_d \approx 100$ mT [solid line in Fig. 4(d)]. The amplitude of this variation is found to depend almost only on the hole shape and not on the ADL period $p$. [We note that, despite the fact that $-H_d > H$, the spins are stabilized in

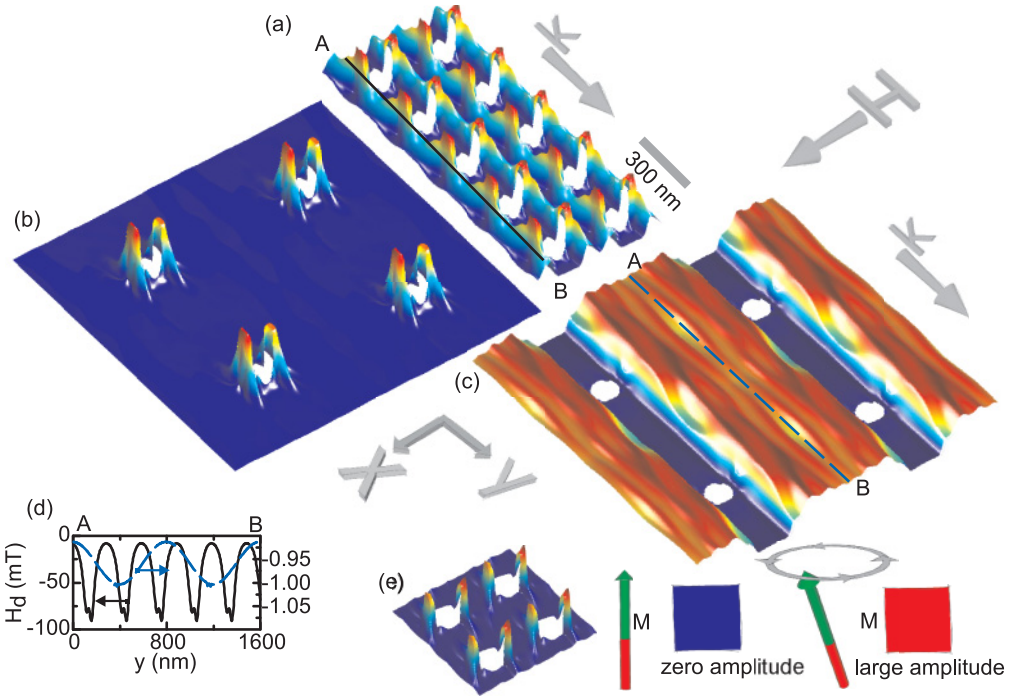


FIG. 4. (Color online) Spatial SW profiles for $\mu_0 H = 40$ mT, $\phi = 1^\circ$, and $k = 0$, simulated for (a) $p = 0.3$ $\mu$m, $f = 2.9$ GHz. (b) $p = 0.8$ $\mu$m, $f = 2.9$ GHz. (c) $p = 0.8$ $\mu$m, $f = 5.6$ GHz. Large (small) precession amplitude corresponds to large (small) $z$ elevation. (d) $x$ component of demagnetization field $H_d$ for $p = 0.3$ $\mu$m (solid line) and $p = 0.8$ $\mu$m (dashed line). $H_d$ is taken in the $y$ direction along the lines (A-B) in (a) and (c), respectively. (e) Spatial SW profile for $p = 0.3$ $\mu$m, $f = 4.5$ GHz, and $\eta = 10^\circ$. The color coding for zero and maximum spin precession amplitude is shown.

their magnetization configuration due to an effective positive contribution of the exchange field.] Considering the very inhomogeneous internal field it is now instructive to identify regions in $H_d(x,y)$ where spins can precess resonantly at $f = 2.9$ GHz. We use theoretical SW dispersion relations from Ref. 18, taking into account a quantization parallel to the field as present in a transversely magnetized wire. We do this in order to identify regions where the excitation is within the spin-wave band.[37,38] By using the values $H_d(x,y)$ obtained by micromagnetic simulations, we substantiate resonant spin precession at $f = 2.9$ GHz to occur only in the minima of $H_d$, very close to the edges of the holes. In the intermediate regions, the nonzero amplitudes reflect off-resonance excitation.

We now interpret our data. The large group velocity $v_g$ found in our experiment using a small-$k$ excitation suggests a steep slope of the spin-wave dispersion relation in the long-wavelength limit [cf. Fig. 5(b)]. For an unpatterned plain permalloy film it is known[18] that, at long wavelengths with $k \lesssim 1 \times 10^5$ rad/cm, the main contribution to the dynamic coupling (susceptibility in resonance) comes from dynamic dipolar coupling. In particular, for Damon-Eshbach modes where $\mathbf{k} \perp \mathbf{M}$ the dynamic dipolar coupling leads to a steep slope in the dispersion relation and thereby a large group velocity $v_g$. In our case we attribute the experimental finding of large $v_g$ to the fact that SWs tunnel between the neighboring resonant oscillators localized at the holes' edges.[38,39] The strength of such dipolar tunneling depends on the tunneling distance, the film thickness, and the susceptibility of the material through which the SW tunnels.[22,23,39] A large susceptibility $\chi$ of a material amplifies the dipolar stray field and thereby increases the dipolar coupling strength (i.e., tunneling probability) between both sides of the tunnel barrier. Our discussion is along the finding of Wang *et al.*,[21,40] where two sets of nanowires of alternating ferromagnetic material formed a ferromagnetic film without air gaps. They observed band formation and a relatively large group velocity in the long-wavelength limit when $\mathbf{k}$ was perpendicular to $\mathbf{M}$. The band formation was attributed to resonant and off-resonant precession of the adjacent ferromagnetic nanowires (see p. 9 of Ref. 23), which exhibited different individual resonance frequencies at a given magnetic field.[22,23] In the ADL geometry considered here, edge-mode SWs tunnel through one-and-the-same ferromagnetic material. Between the holes, spin precession is off-resonance but the material still provides a large $\chi$ due to the nearby resonance. At the same time the material in between provides exchange coupling between modes. This feature of the ADL geometry is different if compared with magnetic elements from one-and-the-same material which are separated by an air gap. [We compare with values of air-gap-separated nanoelements. In Fig. 2 of Ref. 22, for stripes of 70 nm separation, a group velocity of $v_g = 2.8$ km/s is found at $\mu_0 H = 50$ mT and $\approx$10 GHz. Note that the separation is much smaller if compared with the edge mode discussed here for the $p = 300$ nm ADL, where a higher $v_g$ is found. In Ref. 15, discs separated by a 70-nm-wide air gap are studied. In Fig. 5 of Ref. 15, $v_g = 0$ was found for $\mu_0 H = 150$ mT and 6 to 8 GHz, suggesting that dipolar coupling was weak.]

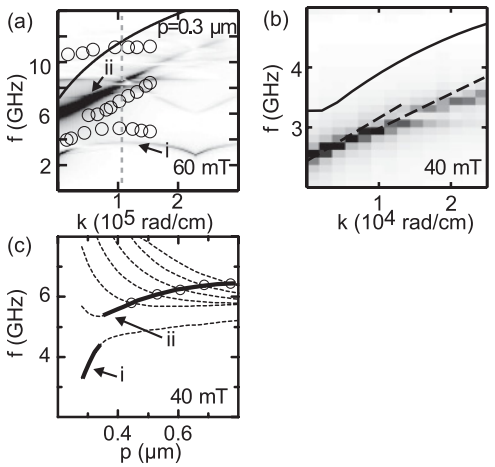


FIG. 5. Dispersions obtained from micromagnetic simulations (gray-scale plot) and BLS measurements (symbols) at $\mu_0 H = 60$ mT. A miniband behavior is resolved at low frequency for $p = 0.3$ $\mu$m. The solid line is the calculated plain-film dispersion for $M_s = 760$ kA/m and film thickness $\delta = 25$ nm. The vertical dashed line indicates the Brillouin zone boundary at $\pi/0.3$ $\mu$m. (b) Zoom into the SW dispersion at $\mu_0 H = 40$ mT near $k = 0$, as obtained from PWM calculations (solid line) and micromagnetic simulations (gray-scale plot). The dashed lines indicate the $v_g$ obtained for $k = 0.5 \times 10^4$ rad/$\mu$m and $k = 1.5 \times 10^4$ rad/$\mu$m. They correspond to $v_g = 4.5$ and $v_g = 3.6$ km/s, respectively. Such data are evaluated to obtain values $v_g$ considered in Fig. 3(b) (see text for details). (c) Mode frequencies calculated by PWM for different $p$. The thick solid lines mark regions where, for $p < 0.35$ $\mu$m the edge mode i and for $p > 0.35$ $\mu$m the extended mode ii is predicted to be the propagating mode. Circles mark predicted mode crossings (see text).

In particular, the FIB technique has allowed us to create short tunneling distances for edge modes and generate large $v_g$ at $p < 0.4$ $\mu$m. For $p = 0.8$ $\mu$m, the large distances between individual holes forbids SW tunneling, and coherence between edge excitations is not induced. In experiments on ADLs with $p \geqslant 0.6$ $\mu$m, we do not resolve mode i experimentally. This is attributed to edge roughness and variations in the hole diameters further decreasing the coherence.[41] Due to variations in the demagnetization field at different holes, the individual resonances differ. Differently to the case of the coupled modes at $p = 0.3$ $\mu$m, where the coupling can phase and frequency lock the individual resonators, the experimental linewidth broadens inhomogeneously.[42] This makes such modes difficult to detect.

We have performed further simulations at a constant field $\mu_0 H = 40$ mT where we have varied $\eta$. We find that, for $\eta \approx 10^\circ$, the regions of large precession amplitude at neighboring holes do not overlap [Fig. 4(e)]. Dipolar coupling is significantly reduced and the edge modes do not support a propagating SW any longer. The simulations suggest $v_g$ becoming zero for increasing $\eta$. This explains the strong anisotropy of $v_g$ depicted in Fig. 3(a). The angular anisotropy of $v_g$ is much less pronounced in the ADL with $p = 0.8$ $\mu$m or a plain film.[18,28] The tunability from very large $v_g$ to zero $v_g$ is thus a unique feature of nanostructured ADLs originating from the coherent magnonic coupling of edge modes.

### C. Magnonic band formation

We now discuss the coupling of edge modes for $p < 0.4$ $\mu$m. We argue that the coupling can be understood in the framework of a tight-binding model of localized states.[43] For such an approach, one expects the SW dispersion $f(k)$ to be periodic in $k$ space and exhibit a Brillouin zone boundary. In Fig. 5(a) we use both wave-vector-resolved SW detection via BLS (open symbols) and micromagnetic simulations (gray-scale plot) to explore the dispersion $f(k)$ for $p = 0.3$ $\mu$m by experimental and theoretical means, respectively. Data are taken at $\mu_0 H = 60$ mT, where the wave-vector-resolved spectra exhibit a good signal-to-noise (SNR) ratio. Three different SW modes are resolved. They correspond to modes i, ii, and iii observed in Figs. 2(a) and 2(b) in ascending order for increasing $f$. Minimum frequency has the edge mode [cf. Fig. 4(a)], mode ii is the extended mode, and mode iii corresponds to a mode localized in between neighboring holes (cf. Figs. 2(b) and 2(d) in Ref. 41). The frequency of the lowest-frequency branch (mode i, edge mode) varies characteristically as a function of $k$ with a frequency maximum at $k \approx 1 \times 10^5$ rad/cm in Fig. 5(a). Interestingly, the Brillouin zone boundary of the ADL as defined by $k_{BZ} = \pi/p = 1.05 \times 10^5$ rad/cm amounts to almost the same value. Beyond the Brillouin zone boundary the frequency decreases again. This is consistent with a miniband being periodic in $k$ space. The slight difference of the simulated Brillouin zone boundary of ≈5% most likely has its origin in the large simulation-unit-cell discretization of 9.75 nm. The miniband bandwidth is 0.6 GHz. In Ref. 44, Dvornik *et al.* studied theoretically the coupling of edge modes in two neighboring 50-nm-wide nanomagnets. In Fig. 3(b) of Ref. 44, the authors reported a mode splitting of about 0.25 GHz (simulated) and 0.05 GHz (analytical result) in case of a dipolar interaction across an air gap. The center-to-center separation of the edge modes was 100 nm. In our case the center-to-center separation of edge modes is three times larger and amounts to 300 nm. Still, we find a large interaction-induced miniband width of about 0.6 GHz. The simulations displayed as a gray-scale plot in Fig. 5(a) remodel our observation of a miniband of the edge-mode excitation. A discrepancy remains in the frequencies. This might be caused by two effects: first, a small misalignment between the magnetic field $H$ and the high-symmetry direction of the ADL and, second, mode i resides close to the hole edges and is influenced by their roughness, which is not modeled.[41]

Extracting $v_g$ from the simulations at $k = k_{CPW} = 0.1 k_{BZ}$ ($\mu_0 H = 40$ mT), we obtain $v_g = 4.2 \pm 0.7$ km/s for $p = 0.3$ $\mu$m. [We provide a large error of 0.7 km/s when reporting $v_g$ from micromagnetic simulations at $p = 0.3$ $\mu$m. This originates from the dependence of the dispersion on the simulation parameters. Not all sample parameters are known precisely from experiment. We have therefore considered $k = 0.5$ and $1.5 \times 10^4$ rad/cm [reflected by the two slopes in Fig. 5(b)], $\delta = 22, \ldots, 25$ nm, and a small out-of-plane anisotropy in the simulation. We note that $v_g$ obtained for the extended mode does not vary much. For the edge mode, however, the parameter variations give a large error, as indicated in Fig. 5(b).] The experimental value of $v_g = 4.8$ km/s measured at $\eta = 2^\circ$ is in good agreement. The large $v_g$ close to $k = 0$ is a result of the miniband formation in magnonic systems (cf. Fig. 2

in Ref. 22). We use an enlarged scale to extract $v_g$ close to zero from the simulated data [see Fig. 5(b)]. We summarize simulated group velocities in Fig. 3(b) as squares for $p$ ranging between 0.3 and 0.8 $\mu$m. These data and the experimentally observed values follow the same trend. AESWS experiments with tailored CPWs thus turn out to be particularly powerful to quantify $v_g$ close to the Brillouin zone center $k = 0$.

In Fig. 5(a), the experimental and simulated data show a clear MC band formation for mode i of Fig. 2(a) (i.e., the edge mode residing at low frequencies). For mode ii of Fig. 2(a) (i.e., the extended mode at higher frequencies), a miniband formation and small forbidden-frequency gap is predicted but much less pronounced. In the simulations of Fig. 5(a) the extended mode exhibits a periodic behavior as a function of $k$, suggesting MC behavior, but the intensity at large $k$ is extremely weak if compared to both the dispersion close to $k = 0$ and the edge mode. Mode ii originates from the undisturbed plain-film mode. It experiences a slight periodic modulation of the internal field [see Fig. 4(d)]. Only very recently have small forbidden-frequency gaps near Brillouin zone boundaries been observed in a detailed BLS experiment at the higher-frequency modes at large $k$. These gaps are out of the scope of this paper and will be discussed elsewhere.[45]

## IV. THEORETICAL ANALYSIS USING PLANE WAVE METHOD

### A. Formalism and basic considerations

In Ref. 24 the plane wave method (PWM) was employed to model 3D magnonic crystals. We modified and used this approach to model 2D antidot lattices. So far, only the dynamic magnetostatic field was included in the PWM. In the present formulation, the nonuniform static dipolar field together with the finite thickness of the considered film are taken into account. Let us consider a slab of a 2D magnonic crystal where the dynamics of magnetization vector $\mathbf{M}(\mathbf{r},t)$ is described by the Landau-Lifshitz (LL) equation with damping neglected,

$$\frac{\partial \mathbf{M}(\mathbf{r},t)}{\partial t} = -\gamma\mu_0[\mathbf{M}(\mathbf{r},t) \times \mathbf{H}_{\text{eff}}(\mathbf{r},t)], \tag{1}$$

where $\gamma$ is the gyromagnetic ratio ($\gamma > 0$), $\mu_0$ is permeability of vacuum, $t$ is the time, and $\mathbf{H}_{\text{eff}}$ is effective magnetic field. $\mathbf{H}_{\text{eff}}$ consist of three terms:

$$\mathbf{H}_{\text{eff}}(\mathbf{r},t) = \mathbf{H}_0 + \mathbf{H}_{\text{ex}}(\mathbf{r},t) + \mathbf{H}_{\text{dip}}(\mathbf{r},t). \tag{2}$$

The first term is the applied magnetic field $H_0$, which is homogeneous in space and directed along the $x$ axis (in the PWM calculations only this one direction will be considered). The next component of the effective field is the exchange field $\mathbf{H}_{\text{ex}}(\mathbf{r},t)$. In magnetically inhomogeneous materials the spatial inhomogeneity of both the exchange constant $A(\mathbf{r})$ and the saturation magnetization $M_s(\mathbf{r})$ must be taken into account, which leads to the following formula:

$$\mathbf{H}_{\text{ex}}(\mathbf{r},t) = \left(\nabla \cdot l_{\text{ex}}^2 \nabla\right) \mathbf{m}(\mathbf{r},t), \tag{3}$$

where the exchange length is defined as $l_{\text{ex}} = [2A/(\mu_0 M_s^2)]^{1/2}$. In a linear approximation for saturated samples we can decompose the magnetization vector into a static and dynamic part:

$$\mathbf{M}(\mathbf{r},t) = M_s\hat{\boldsymbol{e}}_x + \mathbf{m}(\mathbf{r},t), \tag{4}$$

where we assume that the static part of the magnetization vector is parallel to the $x$ axis and is equal to $M_s$. The last component of the effective magnetic field in Eq. (2) is the dipolar field. A computation of this field in magnetic systems is one of the main issues in spin-wave calculations. We start with decomposition of this field into the static and dynamic parts, $\mathbf{H}(\mathbf{r})$ and $\mathbf{h}(\mathbf{r},t)$, respectively. Because we are interested in solutions corresponding to monochromatic spin waves, the time dependencies of the dynamic magnetization and dipolar field take the form $\mathbf{m}(\mathbf{r},t) = \mathbf{m}(\mathbf{r})e^{i\omega t}$ and $\mathbf{h}(\mathbf{r},t) = \mathbf{h}(\mathbf{r})e^{i\omega t}$, respectively, where $\omega = 2\pi f$.

According to the ideas presented in Ref. 46, for a slab of a 2D magnonic crystal with uniform magnetization along its thickness, the Maxwell equations can be solved in the magnetostatic approximation with electromagnetic boundary conditions properly taken into account on both surfaces of the 2D magnonic crystal slab, which are located at $z = -\delta/2$ and $z = \delta/2$. For the structure considered and which is extended to infinity in the $(x,y)$ plane, analytical solutions in the form of a Fourier series can be obtained for both static and dynamic magnetic fields:

$$H_x(\mathbf{r}_\parallel,z) = -\sum_{\mathbf{G}_\parallel} \frac{M_s(\mathbf{G}_\parallel)}{\mathbf{G}_\parallel^2} G_x^2[1 - \cosh(|\mathbf{G}_\parallel|z|)e^{-|\mathbf{G}_\parallel|\delta/2}]e^{i\mathbf{G}_\parallel\cdot\mathbf{r}_\parallel}, \tag{5}$$

$$h_y(\mathbf{r}_\parallel,z) = \sum_{\mathbf{G}_\parallel} \left\{ i\frac{m_z(\mathbf{G}_\parallel)}{|\mathbf{k}_\parallel+\mathbf{G}_\parallel|}(k_y+G_y)\sinh(|\mathbf{k}_\parallel+\mathbf{G}_\parallel|z)e^{-|\mathbf{k}_\parallel+\mathbf{G}_\parallel|\delta/2} - \frac{m_y(\mathbf{G}_\parallel)}{|\mathbf{k}_\parallel+\mathbf{G}_\parallel|^2}(k_y+G_y)^2[1-\cosh(|\mathbf{k}_\parallel+\mathbf{G}_\parallel|z) \times e^{-|\mathbf{k}_\parallel+\mathbf{G}_\parallel|\delta/2}] \right\} e^{i(\mathbf{k}_\parallel+\mathbf{G}_\parallel)\cdot\mathbf{r}_\parallel}, \tag{6}$$

$$h_z(\mathbf{r}_\parallel,z) = \sum_{\mathbf{G}_\parallel} \left[ i\frac{m_y(\mathbf{G}_\parallel)}{|\mathbf{k}_\parallel+\mathbf{G}_\parallel|}(k_y+G_y)\sinh(|\mathbf{k}_\parallel+\mathbf{G}_\parallel|z)e^{-|\mathbf{k}_\parallel+\mathbf{G}_\parallel|\delta/2} - m_z(\mathbf{G}_\parallel)\cosh(|\mathbf{k}_\parallel+\mathbf{G}_\parallel|z)e^{-|\mathbf{k}_\parallel+\mathbf{G}_\parallel|\delta/2} \right] e^{i(\mathbf{k}_\parallel+\mathbf{G}_\parallel)\cdot\mathbf{r}_\parallel}, \tag{7}$$

where $\mathbf{r}_\parallel$ is a position vector in the plane of periodicity and $\mathbf{G}_\parallel = (G_x,G_y)$ denotes a reciprocal lattice vector of our structure [i.e., $\mathbf{G}_\parallel = \frac{2\pi}{p}(n_x,n_y)$; $n_x$ and $n_y$ are integers]. $M_s(\mathbf{G}_\parallel)$ are Fourier components of saturation magnetization, which are calculated analytically for the circular shape of antidots. $\mathbf{k}_\parallel = (k_x,k_y)$ is a Bloch wave vector of spin waves which, according to the Bloch theorem, can be limited to the first Brillouin zone. In deriving Eqs. (6) and (7) we use the Bloch theorem for dynamical components:

$$\mathbf{m}(\mathbf{r}) = \sum_{\mathbf{G}_\parallel} \mathbf{m}(\mathbf{G}_\parallel)e^{i(\mathbf{k}_\parallel+\mathbf{G}_\parallel)\cdot\mathbf{r}_\parallel}, \quad \mathbf{h}(\mathbf{r}) = \sum_{\mathbf{G}_\parallel} \mathbf{h}(\mathbf{G}_\parallel)e^{i(\mathbf{k}_\parallel+\mathbf{G}_\parallel)\cdot\mathbf{r}_\parallel}, \tag{8}$$

and assume that the static demagnetizing field is parallel to the spontaneous magnetization.

The formulas obtained for the demagnetizing fields are represented in the reciprocal space for the in-plane components but depend on the position along the thickness of the slab. However, when the slab is thin enough (which is the case for the ADL discussed with $\delta = 25 \pm 3$ nm), the nonuniformity of the demagnetizing fields across its thickness can be neglected and respective values of fields from Eqs. (6) and (7) with $z = 0$ are used in the calculations. Because of its Fourier-series form, the solution found for the demagnetizing fields can be used directly in the PWM technique described in Ref. 24. After applying the plane wave method to the LL equation (1) and using the solutions (6) and (7) for the dipolar field, one can obtain the algebraic eigenvalue problem which can be solved numerically.

Modeling of nonmagnetic material in PWM-based calculations of magnonic spectra has not been possible so far. This is due to the formulation of the equation of motion, the LL equation, for inhomogeneous media. In nonmagnetic media the magnetization is zero and the LL equation becomes an identity. However, in the PWM the system dynamics is described by a superposition of a number of plane waves, which are continuous functions and propagate throughout the medium. Thus, each plane wave must be defined also in the nonmagnetic medium. To do so, we model the holes by a region of strongly reduced $M_s$. Then the set of solutions are subdivided into physical and nonphysical results: physical (nonphysical) solutions have close to zero (almost infinite) precession amplitude within the holes represented by reduced $M_s$. Material parameters are chosen to eliminate the nonphysical solutions from the relevant frequency range without affecting the frequencies of the proper (physical) modes.

For the holes, we use a value of $M_s$ at least ten times lower than in permalloy to reproduce the shape and value of the static demagnetizing field with good accuracy (less than 10% error). This causes the nonphysical solutions localized within the holes to shift to high frequencies.[18] For $p = 0.3$ $\mu$m, only the fifth mode (in increasing frequency order) has a sensible amplitude in the hole region, and thus represents a nonphysical solution.

The relevance of this formalism goes beyond the system of magnonic crystals: similar challenges are encountered in the application of the PWM to the calculation of band structures of phononic crystals consisting of a solid and a liquid or gas.[47,48] Similarly to the SWs confined to magnetic material in the MC, in phononic crystals transverse vibrations do not occur in constituting liquids and gases. The abrupt vanishing of these vibrations at the border between the solid and the gas leads to nonphysical extra solutions in the PWM.

### B. Plane wave method applied to antidot lattices of different periodicity

Using the PWM we calculated the relevant modes with zero precession amplitude within the holes (i.e., physical solutions), and we show the corresponding field dispersions in Fig. 2(b) as solid lines. Note that we have plotted only symmetric modes in order to consider the excitation symmetry in AESWS.[29] The PWM results and the experimental data are in good agreement. Spatial mode profiles calculated by the PWM (not shown) for modes i, ii, and iii agree well with micromagnetic simulations [cf. Fig. 4]. We have thus verified by PWM the occurrence and spatial profiles of the relevant modes in the ADLs.

The PWM allows us to elucidate the dependence of propagation characteristics on $p$. In Fig. 5(b), we have plotted the frequency of the relevant modes as a function of ADL periodicity $p$. The thick lines mark the mode with largest $v_g$. For $p < 0.35$ $\mu$m, we find that the edge mode (mode i) propagates. At $p = 0.35$ $\mu$m, the theory predicts a transition to occur in that the mode ii (i.e., the extended mode) is found to propagate for large $p$. Our experiments are consistent with this transition. In particular, we observe the two different propagating modes in one-and-the-same ADL with $p = 0.4$ $\mu$m. [In the PWM we find the extended modes to hybridize with transversally quantized modes for certain $p$, which are highlighted by open circles in Fig. 5(b). We extracted $v_g$ only for specific values of $p$ away from these points of hybridization; namely, $k = k_{CPW}$ for $p = 0.3$, $p = 0.6$, and $p = 0.8$ $\mu$m. The repulsion of the dispersion curves will appear only when the crossing modes have the same symmetry. The mode with largest $v_g$, as excited in the experiment, is symmetric. This means that the crossing at $p$ around 0.44, 0.62, and 0.78 $\mu$m will change neither the dispersion nor the group velocity. When repulsion between dispersion curves exists, the flattening of the dispersion results in a decrease in $v_g$. For experiments, it is challenging to realize an ADL with exactly the correct $p$ to create hybridization. We do not consider this situation here.] Results from PWM are depicted as triangles in Fig. 3(b) and are in good agreement with the simulation and the experimental data. PWM-calculated velocities are systematically larger than the experimental velocities. This discrepancy is attributed to the misalignment angle $\eta - \phi$, which is assumed to be zero in the PWM calculations but ranges from $1^\circ$ to $2^\circ$ in the experiments depicted in Fig. 3(b). Note the good agreement between the value $v_g = 5.8$ km/s obtained by PWM at $p = 0.3$ $\mu$m and the maximum $v_g \approx 6$ km/s obtained by AESWS in Fig. 3(a).

## V. CONCLUSION

In conclusion, we have reported artificial crystal behavior in a nanopatterned antidot lattice. By means of focused ion beam etching we have fabricated arrays of closely spaced nanoholes provoking dynamic coupling of localized resonant spin-wave modes. Dipolar coupling of edge modes is found to create minibands with surprisingly large propagation velocities. We have adapted the plane wave method to describe the devices and reproduce the experimental findings. The large spin-wave velocities create interesting perspectives in the field of nanoscale magnonic devices.

## ACKNOWLEDGMENTS

The research leading to these results has received funding from the European Community's Seventh Framework Programme (FP7/2007-2013) under Grant No. 228673 (MAGNONICS), the German Excellence Cluster Nanosystems Initiative Munich (NIM), and the Ministero per l'Università e la Ricerca under PRIN-2007 project (Prot. 2007X3Y2Y2).

*grundler@ph.tum.de


[1] R. L. Stamps, Adv. Funct. Mater. **20**, 2380 (2010).

[2] S. Neusser and D. Grundler, Adv. Mater. **21**, 2927 (2009).

[3] B. K. Kuanr, L. M. Malkinski, M. Yu, D. Scherer, R. Camley, and Z. Celinski, in *NSTI Nanotech.*, Vol. 1 (Technical proceedings of the 2008 NSTI Nanotechnology Conference and Trade Show, Boston), edited by M. Laudon and B. Romanowicz (CRC Press, Boca Raton, 2008), pp. 542–545.

[4] A. Khitun, M. Bao, and K. L. Wang, J. Phys. D **43**, 264005 (2010).

[5] Y. Gulyaev, S. Nikitov, L. Zhivotovskii, A. Klimov, P. Tailhades, L. Presmanes, C. Bonningue, C. Tsai, S. Vysotskii, and Y. Filimonov, JETP Lett. **77**, 567 (2003).

[6] V. V. Kruglyak, S. O. Demokritov, and D. Grundler, J. Phys. D **43**, 264001 (2010).

[7] J. D. Joannopoulos *et al.*, *Photonic Crystals: Molding the Flow of Light*, 2nd ed. (Princeton University Press, Princeton, New Jersey, USA, 2008).

[8] H. Gao, W. Zhou, and T. W. Odom, Adv. Funct. Mater. **20**, 529 (2010).

[9] J.-K. Yu, S. Mitrovic, D. Tham, J. Varghese, and J. R. Heath, Nature Nanotech. **5**, 718 (2010).

[10] G. Gubbiotti, M. Madami, S. Tacchi, G. Carlotti, and T. Okuno, J. Appl. Phys. **99**, 08C701 (2006).

[11] G. Gubbiotti, S. Tacchi, G. Carlotti, N. Singh, S. Goolaup, A. O. Adeyeye, and M. Kostylev, Appl. Phys. Lett. **90**, 092503 (2007).

[12] L. Giovannini, F. Montoncello, and F. Nizzoli, Phys. Rev. B **75**, 024416 (2007).

[13] K.-S. Lee, D.-S. Han, and S.-K. Kim, Phys. Rev. Lett. **102**, 127202 (2009).

[14] J. Topp, D. Heitmann, M. P. Kostylev, and D. Grundler, Phys. Rev. Lett. **104**, 207205 (2010).

[15] S. Tacchi, M. Madami, G. Gubbiotti, G. Carlotti, H. Tanigawa, T. Ono, and M. P. Kostylev, Phys. Rev. B **82**, 024401 (2010).

[16] K. Perzlmaier, G. Woltersdorf, and C. H. Back, Phys. Rev. B **77**, 054425 (2008).

[17] J. Jorzick, S. O. Demokritov, C. Mathieu, B. Hillebrands, B. Bartenlian, C. Chappert, F. Rousseaux, and A. N. Slavin, Phys. Rev. B **60**, 15194 (1999).

[18] B. Kalinikos and A. Slavin, J. Phys. C **19**, 7013 (1986).

[19] A. V. Chumak, A. A. Serga, B. Hillebrands, and M. P. Kostylev, Appl. Phys. Lett. **93**, 022508 (2008).

[20] A. V. Chumak, T. Neumann, A. A. Serga, B. Hillebrands, and M. P. Kostylev, J. Phys. D **42**, 205005 (2009).

[21] Z. K. Wang, V. L. Zhang, H. S. Lim, S. C. Ng, M. H. Kuok, S. Jain, and A. O. Adeyeye, ACS Nano **4**, 643 (2010).

[22] M. P. Kostylev and A. A. Stashkevich, Phys. Rev. B **81**, 054418 (2010).

[23] G. Gubbiotti, S. Tacchi, M. Madami, G. Carlotti, A. O. Adeyeye, and M. Kostylev, J. Phys. D **43**, 264003 (2010).

[24] M. Krawczyk and H. Puszkarski, Phys. Rev. B **77**, 054437 (2008).

[25] S. S. Kalarickal, P. Krivosik, M. Wu, C. E. Patton, M. L. Schneider, P. Kabos, T. J. Silva, and J. P. Nibarger, J. Appl. Phys. **99**, 093909 (2006).

[26] M. Bailleul, D. Olligs, and C. Fermon, Appl. Phys. Lett. **83**, 972 (2003).

[27] Z. Liu, F. Giesen, X. Zhu, R. D. Sydora, and M. R. Freeman, Phys. Rev. Lett. **98**, 087201 (2007).

[28] S. Neusser, G. Durr, H. G. Bauer, S. Tacchi, M. Madami, G. Woltersdorf, G. Gubbiotti, C. H. Back, and D. Grundler, Phys. Rev. Lett. **105**, 067208 (2010).

[29] F. Giesen, J. Podbielski, T. Korn, and D. Grundler, J. Appl. Phys. **97**, 10A712 (2005).

[30] D. V. Berkov and N. L. Gorn, *Micromagus—Software for Micromagnetic Simulations* (2008), [http://www.micromagus.de].

[31] M. J. Pechan, C. Yu, R. L. Compton, J. P. Park, and P. A. Crowell, J. Appl. Phys. **97**, 10J903 (2005).

[32] S. Neusser, B. Botters, and D. Grundler, Phys. Rev. B **78**, 087825 (2008).

[33] M. Kostylev, G. Gubbiotti, G. Carlotti, G. Socino, S. Tacchi, C. Wang, N. Singh, A. O. Adeyeye, and R. L. Stamps, J. Appl. Phys. **103**, 07C507 (2008).

[34] S. Tacchi, M. Madami, G. Gubbiotti, G. Carlotti, A. Adeyeye, S. Neusser, B. Botters, and D. Grundler, IEEE Trans. Magn. **46**, 172 (2010).

[35] S. Tacchi, M. Madami, G. Gubbiotti, G. Carlotti, A. O. Adeyeye, S. Neusser, B. Botters, and D. Grundler, IEEE Trans. Magn. **46**, 1440 (2010).

[36] V. E. Demidov, M. Buchmeier, K. Rott, P. Krzysteczko, J. Münchenberger, G. Reiss, and S. O. Demokritov, Phys. Rev. Lett. **104**, 217203 (2010).

[37] A. Gurevich and G. Melkov, *Magnetization Oscillations and Waves* (CRC Press, Boca Raton, Florida, USA, 1996).

[38] M. P. Kostylev and N. A. Sergeeva, *Collective and Individual Modes on One-Dimensional Bi-layered Magnetic Structures* (Transworld Research Network, T.C., Trivandrum, Kerala, India, 2006).

[39] S. O. Demokritov, A. A. Serga, A. André, V. E. Demidov, M. P. Kostylev, B. Hillebrands, and A. N. Slavin, Phys. Rev. Lett. **93**, 047201 (2004).

[40] Z. K. Wang, V. L. Zhang, H. S. Lim, S. C. Ng, M. H. Kuok, S. Jain, and A. O. Adeyeye, Appl. Phys. Lett. **94**, 083112 (2009).

[41] S. Neusser, B. Botters, M. Becherer, D. Schmitt-Landsiedel, and D. Grundler, Appl. Phys. Lett. **93**, 122501 (2008).

[42] S. Kaka, M. R. Pufall, W. H. Rippard, T. J. Silva, S. E. Russek, and J. A. Katine, Nature (London) **437**, 389 (2005).

[43] J. C. Slater and G. F. Koster, Phys. Rev. **94**, 1498 (1954).

[44] M. Dvornik, P. V. Bondarenko, B. A. Ivanov, and V. V. Kruglyak, J. Appl. Phys. **109**, 07B912 (2011).

[45] R. Zivieri, S. Tacchi, F. Montoncello, L. Giovannini, F. Nizzoli, M. Madami, G. Gubbiotti, G. Carlotti, S. Neusser, G. Duerr *et al.* (unpublished).

[46] J. Kaczer and L. Murtinova, Phys. Status Solid A **23**, 79 (1974).

[47] C. Goffaux and J. P. Vigneron, Phys. Rev. B **64**, 075118 (2001).

[48] Y. Pennec, J. O. Vasseur, B. Djafari-Rouhani, L. Dobrzynski, and P. A. Deymier, Surf. Sci. Rep. **65**, 229 (2010).